

# A Jellium Model for the Anomalous Hall Crystal

Tomohiro Soejima (副島智大),<sup>1,\*</sup> Junkai Dong (董俊楷),<sup>1,2,\*</sup> Ashvin Vishwanath,<sup>1</sup> and Daniel E. Parker<sup>3</sup>

<sup>1</sup>*Department of Physics, Harvard University, Cambridge, MA 02138, USA*

<sup>2</sup>*Kavli Institute for Theoretical Physics, University of California, Santa Barbara, California 93106, USA*

<sup>3</sup>*Department of Physics, University of California at San Diego, La Jolla, California 92093, USA*

The jellium model is a paradigmatic problem in condensed matter physics, exhibiting a phase transition between metallic and Wigner crystal phases. However, its vanishing Berry curvature makes it ill-suited for studying recent experimental platforms that combine strong interactions with nontrivial quantum geometry. These experiments inspired the anomalous Hall crystal (AHC) — a topological variant of the Wigner crystal. The AHC spontaneously breaks continuous translation symmetry but has a nonzero Chern number. In this work, we introduce  $\lambda$ -jellium, a minimal extension of the two-dimensional jellium model. Its Berry curvature distribution is controlled by a single parameter,  $\lambda$ , where  $\lambda = 0$  corresponds to the standard jellium model. This setup facilitates the systematic exploration of Berry curvature's impact on electron crystallization. The phase diagram of this model, established using self-consistent Hartree Fock calculations, reveals several interesting features: (i) The AHC phase occupies a large region of the phase diagram. (ii) Two distinct Wigner crystal phases, the latter enabled by quantum geometry, and two distinct Fermi liquid phases are present. (iii) A continuous phase transition separates the AHC and one of the WC phases. (iv) In some parts of the AHC phase, the lattice geometry is non-triangular, unlike in the classical Wigner crystal. In addition to elucidating the physics of correlated electrons with nonzero Berry curvature, we expect that the simplicity of the model makes it an excellent starting point for more advanced numerical methods.

## I. INTRODUCTION

In the classic problem considered by Wigner [1], electron crystallization driven by strong Coulomb interactions was examined within the jellium model, in which an electron fluid embedded in a uniform neutralizing background spontaneously breaks translation symmetry upon decreasing the density. The two-dimensional incarnation of the jellium model, the two-dimensional electron gas (2DEG), has since been studied extensively using advanced numerical techniques [2–13], which revealed the importance of beyond-mean-field effects for the energy competition of the Wigner crystal (WC) phase with the Fermi liquid.

Recent experiments [14–17] in rhombohedral multi-layer graphene (RMG), where new phases including integer and fractional quantum Hall phases emerge at low electronic densities and zero magnetic field, have inspired an explosion of theoretical interest in topological crystalline phases of matter. We, along with our collaborators and other simultaneous works, proposed [18–20] the possibility of an interaction-driven Chern insulator that spontaneously breaks continuous translation symmetry, which we dubbed the anomalous Hall crystal (AHC).

The complexity of the microscopic RMG Hamiltonian, consisting of ten orbitals and a morass of single particle hopping parameters, makes it difficult to distill simple physics, preventing a unified understanding despite intensive efforts [21–28]. This has led to a flurry of interest in simplified models for AHCs [29–31]. However, these models are either phenomenological mean-field models,

or contain a large number of spinor components, thus precluding the possibility of beyond mean-field numerics. Indeed, determining the fate of the AHC in the presence of beyond-mean-field quantum fluctuations is an urgent challenge.

To begin tackling this challenge, we propose a simple model:  $\lambda$ -jellium. This two-band model endows the quadratic band of the jellium model with a nontrivial skyrmionic texture in momentum space, which is responsible for its non-zero Berry curvature. The model contains two tuning parameters:  $r_s$  and  $\lambda$ . The familiar  $r_s$  is the ratio between the quadratic dispersion and Coulomb interaction terms, whereas  $1/\lambda$  controls the extent of the skyrmionic texture. In the  $\lambda \rightarrow 0$  limit, the model reduces to the standard two-dimensional jellium model, thus allowing us to systematically understand the effect of Berry curvature. Our model, given its simplicity, limited spinor dimensions, and connection to the jellium model, can be studied with beyond mean-field techniques employed such as variational and diffusion Monte-Carlo methods developed over many decades [3–12].

To pave the way for these advanced methods, we perform extensive self-consistent Hartree-Fock calculations of the phase diagram of the  $\lambda$ -jellium model. We find that the AHC phase occupies a significant region of the phase diagram. In addition, we also find two distinct Wigner crystal phases, a conventional Wigner crystal and a halo Wigner crystal with distinct symmetry properties. Two Fermi liquids, whose Fermi surfaces are circular and annular, also appear in the phase diagram. We find that the halo Wigner crystal and the annular Fermi liquid arises due to the interplay between interactions and non-trivial quantum geometry. We further find a quantum critical point between the AHC phase and the halo Wigner crys-

\* These authors contributed equally.

tal, which is described by an emergent Dirac cone.

Finally, we find that in some parts of the AHC phase, the lattice geometry can be non-triangular. This subtlety in the choice of lattice geometry already exists in the case of Wigner crystals, where the large  $r_s$  classical electrostatic limit selects the triangular lattice. However, deep in the quantum regime, the preferred lattice geometry is not *a priori* clear. For instance, with spinful electrons at small interaction strengths, a square antiferromagnet wins over the triangular lattice within HF [13]. Similarly, in  $\lambda$ -jellium we find that non-triangular AHC states can be energetically preferred over triangular AHC states. This echoes earlier works on RMG, which found unit cells with multiple electrons [16, 26] or non-triangular unit cells [32] can be stabilized.

The rest of the paper is organized as follows. Section II introduces the  $\lambda$ -jellium model. Sec. III, then analyzes its mean-field phase diagram in detail. In Sec. IV, we examine the second-order phase transition between the AHC and WC. Sec. V examines the close competition within the AHC phase between triangular and square unit cells. Finally, we close with a discussion in Sec. VI.

## II. THE $\lambda$ -JELLIUM MODEL

We now introduce the Hamiltonian for  $\lambda$ -jellium, a two-band generalization of jellium with a skyrmionic texture in momentum space that provides a tunable amount of Berry curvature.

Recall the Hamiltonian for the (spinless) 2DEG is [4]

$$\hat{H}_{2\text{DEG}} = \frac{1}{r_s^2} \sum_{i=1}^N \nabla_i^2 + \frac{2}{r_s} \sum_{i < j}^N \frac{1}{|\mathbf{r}_i - \mathbf{r}_j|}, \quad (1)$$

where length is measured in units of the typical interparticle distance  $a$  (defined below), and energy has units of Rydbergs Ry [33]. These are related to microscopic units by [4]

$$r_s = \frac{a}{a_0}, \quad a = \frac{1}{\sqrt{\pi\rho}}, \quad a_0 = \frac{\hbar^2}{me^2}, \quad \text{Ry} = \frac{me^4}{2\hbar^2}. \quad (2)$$

Here  $\rho$  is the number density of electrons, a circle of radius  $a$  encloses one particle on average, and  $r_s$  is the dimensionless potential/kinetic ratio. Eq. (2) sets the Fermi momentum to be  $k_F = \frac{2}{a}$ .

We now present a *local* two-band generalization of this model whose lower band has identical dispersion and interaction to Eq. (1), but includes a tunable amount of Berry curvature concentrated at the band minimum. To maintain locality, we use a kinetic energy that is a simple polynomial in the derivative operators:

$$\hat{h} = \Delta \begin{bmatrix} -\lambda^2 \nabla^2 & i\lambda\partial \\ i\lambda\bar{\partial} & 1 \end{bmatrix}, \quad (3)$$

where  $\partial = \partial_x - i\partial_y$ ,  $\nabla^2 = \partial_x^2 + \partial_y^2$  and  $\Delta$  is a large and positive constant. One can think of this as a Dirac

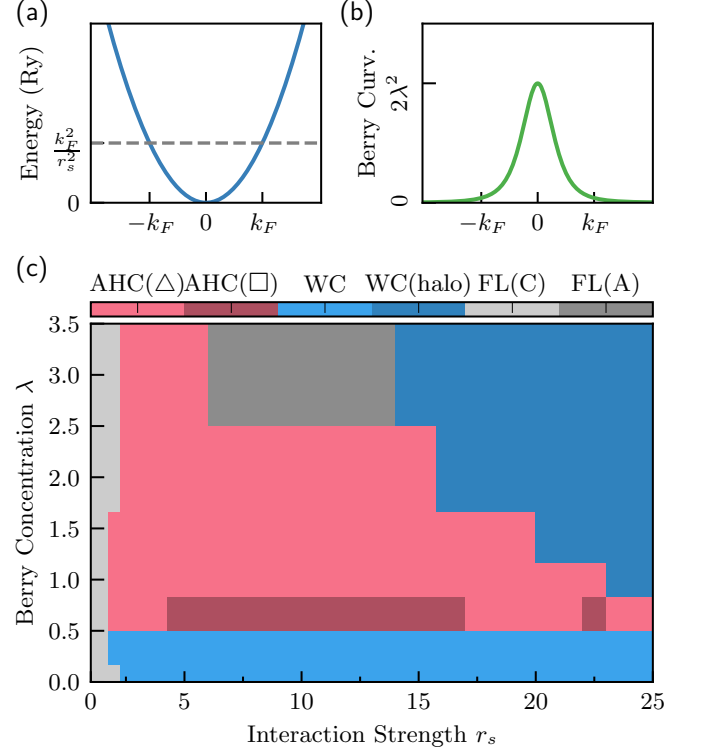


FIG. 1. (a) Quadratic dispersion and (b) Berry curvature of the lower single-particle band of the topological electron gas model, Eq. (5). (c) Mean-field phase diagram. The limit  $\lambda = 0$  is identical to the spinless 2DEG. Two significant Fermi liquid (FL) regions are present: one at low interaction strengths, and one at large interaction strength and Berry curvature concentration. Under strong interactions, a Wigner crystal (WC) appears that undergoes a first-order transition to an anomalous Hall crystal (AHC) at  $\lambda \approx \frac{1}{2}$ . A putative second order transition back to a WC appears at larger  $\lambda$ . A significant region of AHC is present, with the competition between triangular and square AHCs shown by light pink (AHC( $\Delta$ )) when the triangular AHC has lower energy than the square, and dark pink (AHC( $\square$ )) when the reverse is true. Within the AHC phase, a square unit cell is preferred to a triangular unit cell in a region near  $\lambda = 2/3$ .

equation with a momentum-dependent mass. The lower band of  $\hat{h}$  is exactly flat:  $\epsilon_{\mathbf{q}} = 0$ . Its wavefunction is  $\phi(\mathbf{r}) = \frac{1}{\sqrt{A}} \int d^2\mathbf{q} \phi_{\mathbf{q}} e^{i\mathbf{q}\cdot\mathbf{r}}$  with spinor

$$\phi_{\mathbf{q}} = \frac{1}{\sqrt{1 + \lambda^2 q^2}} \begin{bmatrix} 1 \\ \lambda(q_x + iq_y) \end{bmatrix}, \quad (4)$$

where  $q = |\mathbf{q}|$ . The upper band is separated by a gap with minimum size  $\Delta$ . Henceforth we take  $\Delta \rightarrow \infty$  and focus on the lower band.

We combine Eqs. (1,3) to form the full model, which

we call  $\lambda$ -jellium:

$$\hat{H} = \Delta \sum_{i=1}^N \begin{bmatrix} -\lambda^2 \nabla_i^2 & i\lambda \partial_i \\ i\lambda \bar{\partial}_i & 1 \end{bmatrix} - \sum_{i=1}^N \hat{I}_2 \frac{\nabla_i^2}{r_s^2} + \frac{2}{r_s} \sum_{i < j}^N \frac{1}{|\mathbf{r}_i - \mathbf{r}_j|}, \quad (5)$$

where  $\hat{I}_2$  is the identity in spinor space and the interaction is spinor isotropic. We fix the number density to be  $\rho$ ; Eq.(2) applied unchanged. This Hamiltonian is controlled by two dimensionless parameters: the familiar potential/kinetic ratio  $r_s$  and a new parameter  $\lambda$  that controls the concentration of Berry curvature in the lower band.

Let us set out the single-particle properties of  $\lambda$ -jellium. In addition to continuous translation symmetry, the Hamiltonian has a continuous rotation symmetry

$$\hat{R}_\theta \phi(\mathbf{r}) = \begin{pmatrix} 1 & 0 \\ 0 & e^{i\theta} \end{pmatrix} \phi(R_\theta \mathbf{r}), \quad (6)$$

where the 2 by 2 matrix acts on the spinor components. Its single-particle energy is purely kinetic, with dispersion (Fig. 1a)

$$\epsilon_{\mathbf{q}} = \frac{q^2}{r_s^2} \quad (7)$$

in the lower band, matching the 2DEG. The non-trivial spinor  $\phi_{\mathbf{q}}$  gives the lower band a skyrmionic texture in momentum space, with a spin up “skyrmion core” near  $\mathbf{q} = 0$  and spin down at infinity. It wraps the Bloch sphere exactly once as  $\mathbf{q}$  varies, producing Berry curvature (Fig. 1b)

$$\Omega(\mathbf{q}) = 2 \left( \frac{\lambda}{\lambda^2 |\mathbf{q}|^2 + 1} \right)^2. \quad (8)$$

Within a disk of radius  $\kappa$ , the enclosed Berry curvature is a Lorentzian

$$I(\kappa) = 2\pi \frac{\lambda^2 \kappa^2}{1 + \lambda^2 \kappa^2}, \quad (9)$$

with full-width half-max  $\frac{1}{\lambda}$ . As  $\lambda$  grows, the total Berry curvature is always  $2\pi$ , but becomes concentrated at  $\mathbf{q} = 0$ , reaching  $I(k_F = 2/a) = \pi$  at  $\lambda = \frac{1}{2}$ . The Berry curvature vanishes when  $\lambda = 0$ , whereupon the lower band of  $\hat{H}$  reduces to the spinless 2DEG.  $\lambda$ -jellium therefore provides a minimal modification to the standard 2DEG whose interaction strength and band topology can be tuned continuously and independently.

We note that due to the holomorphicity of the unnormalized spinors  $\sqrt{1 + \lambda^2 q^2} \phi_{\mathbf{q}}$  with respect to  $\mathbf{k}$ , the lower band of our continuum  $\lambda$ -jellium model has “ideal quantum geometry” [34, 35]. Another model for the AHC, the parent band model [30], also possesses ideal quantum geometry due to its (anti-)holomorphic spinors. However, the parent band model is usually studied in the limit where the dimension of the spinors becomes large and the Berry curvature becomes uniform. In contrast, the  $\lambda$ -jellium model always has two-component spinors with concentrated Berry curvature around  $\mathbf{k} = 0$ .

### III. MEAN-FIELD PHASE DIAGRAM

We now study the phase diagram of  $\lambda$ -jellium where we find a Berry-curvature induced anomalous Hall crystal competing with other crystalline phases and liquids. We work at mean-field level, employing self-consistent Hartree Fock (SCHF) with three possible translation patterns imposed: (I) continuous translation symmetry (CTS), (II) a discrete translation symmetry (DTS) with a triangular lattice with one electron per unit cell, (III) discrete translation symmetry (DTS) with a *square* lattice with one electron per unit cell. The calculation with CTS is performed in the thermodynamic limit, while the DTS calculation is done on  $N_k \times N_k$  unit cells, with  $N_k$  going up to 36. See Appendices for further numerical details. The resulting phase diagram is shown in Fig. 1 (c).

The long-ranged Coulomb interaction makes energy convergence with the system size difficult. We incorporate the standard correction from the Madelung energy, which effectively reduces the energy error scaling from  $N_k^{-1}$  to  $N_k^{-3}$  [36]. Details of this finite-size scaling can be found in Apps. B,C,D.

We caution that Fermi liquids and crystals compete on an emergent energy scale several orders of magnitude below the interaction scale. Ultimately, beyond-mean-field effects are expected to substantially reshape the phase diagram of  $\lambda$ -jellium, just as they do in the 2DEG, pushing the spinless WC transition from  $r_s^* \sim 2$  to  $r_s^* \sim 30$  [10, 12]. We expect that, as in the 2DEG, mean field theory need not capture phase boundaries accurately but will correctly detect what phases may appear. We now embark on a tour of the phase diagram.

#### A. Circular and Annular Fermi Liquids

The phase diagram (Fig. 1 (c)) supports two regions with Fermi liquid ground states. These two regions correspond to physically distinct Fermi liquids, whose energy competition is driven by the presence of Berry curvature.

To understand the competition between the Fermi liquids, we analyze the phase diagram while imposing continuous translation symmetry. The mean field states are entirely characterized by their momentum space occupations  $n(\mathbf{k}) = \langle c_{\mathbf{k}}^\dagger c_{\mathbf{k}} \rangle$  with *unbounded* momentum  $\mathbf{k}$ . At small  $\lambda$ , we find the textbook circular Fermi liquid, with  $n(\mathbf{k}) = \theta(|\mathbf{k}| - k_F)$ . At moderate interaction strengths,  $\lambda$  drives a transition to an annular Fermi liquid. This phase has two concentric circular Fermi surfaces, so that  $n(\mathbf{k}) = 1$  when  $k_m \leq |\mathbf{k}| \leq k_M$  and otherwise vanishes. The competition between the circular and annular Fermi liquids, which we call FL(C) and FL(A) respectively, is shown in Fig. 2(a).

Interactions drive the formation of the annular Fermi liquid via a mechanism that can be understood qualitatively from the skyrmionic spinor texture. To understand this, let us write down the energy functional for mean-

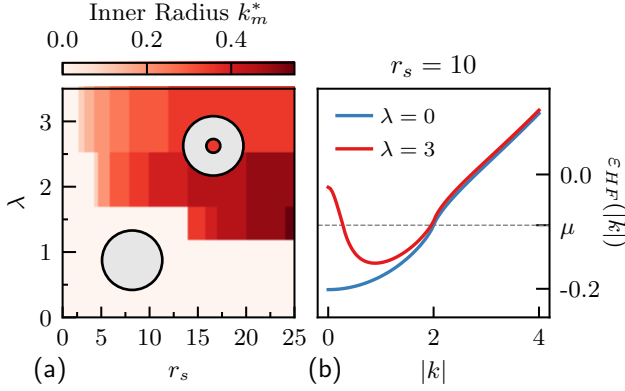


FIG. 2. Fermi liquid phenomenology of the model. (a) Self-consistent inner radius  $k_m^*$  of the Fermi surface when continuous translation symmetry is imposed. (b) The Fermi liquid develops a strong peak at  $\mathbf{k} = 0$  at large  $\lambda, r_s$  due to exchange (Fock) interactions, leading to annular Fermi surfaces.

field Fermi liquid states in terms of  $n(\mathbf{k})$ . The kinetic energy is

$$E_{\text{kin}} = \sum_{\mathbf{k}} n(\mathbf{k}) \frac{|\mathbf{k}|^2}{r_s^2}. \quad (10)$$

As detailed in App. A the interaction projected into the lower band is

$$H_{\text{int}} = \frac{1}{2A} \sum_{\mathbf{q} \neq 0} \sum_{\mathbf{k}, \mathbf{k}'} V(\mathbf{q}) \Lambda_{\mathbf{q}}(\mathbf{k}) \Lambda_{-\mathbf{q}}(\mathbf{k}') : c_{\mathbf{k}}^\dagger c_{\mathbf{k}+\mathbf{q}} c_{\mathbf{k}'}^\dagger c_{\mathbf{k}'-\mathbf{q}} : \quad (11)$$

where  $\Lambda_{\mathbf{q}}(\mathbf{k}) = \phi_{\mathbf{k}}^\dagger \phi_{\mathbf{k}+\mathbf{q}}$  is the form factor and  $V(\mathbf{q}) = 4\pi/r_s |\mathbf{q}|$  is the Fourier transform of the Coulomb interaction. Using Wick's theorem with  $n(\mathbf{k})$

$$E_{\text{int}} = -\frac{1}{2A} \sum_{\mathbf{k}, \mathbf{k}'} \tilde{V}(\mathbf{k}, \mathbf{k}') n(\mathbf{k}) n(\mathbf{k}'), \quad (12)$$

where  $\tilde{V}(\mathbf{k}, \mathbf{k}') = V(\mathbf{k} - \mathbf{k}') |\Lambda_{\mathbf{k}-\mathbf{k}'}(\mathbf{k}')|^2$ . The Hartree-Fock bandstructure for  $n(\mathbf{k})$  is therefore

$$E_{HF}(\mathbf{k}) = \frac{|\mathbf{k}|^2}{r_s^2} - \frac{1}{A} \sum_{\mathbf{k}'} \tilde{V}(\mathbf{k}, \mathbf{k}') n(\mathbf{k}'). \quad (13)$$

We can now qualitatively understand how the spinors control the Hartree-Fock band structure. A nontrivial form factor  $|\Lambda| < 1$  will reduce the exchange energy gain from the Fock term. This is consistent with the fact that exchange interaction favors ferromagnetic spinor configurations. How does this work with the skyrmionic spinor texture Eq. (4)? At small  $\lambda$  the “skyrmion core” region, where spins point up, is large compared to  $k_F$ . The form factors are therefore close to unity, giving a large negative exchange energy. Conversely, large  $\lambda$  spinors have a small

“skyrmion core” compared to  $k_F$ , with most states inside the non-interacting Fermi surface are pointing down. Occupying the mis-aligned spinors near the core incurs a significant energy penalty. This drives the state to deplete the skyrmion core, resulting in an annular Fermi surface, Fig. 2(a). The depletion of  $\mathbf{k} = 0$  will be a recurring feature throughout the phase diagram.

## B. Halo Wigner Crystals

Wigner crystal phases are characterized by spontaneous breaking of continuous symmetry, as well as zero Chern number. The 2DEG is known to host triangular Wigner crystalline states at large  $r_s$  [37–39]. Mean-field calculations underestimate the value of critical  $r_s$  between ferromagnetic FL and WC to be around 2 [13]. The  $\lambda$ -jellium model phase diagram, which is continuously connected to 2DEG in the  $\lambda \rightarrow 0$  limit, also hosts Wigner crystalline phases, shown in Fig. 1(c).

At large  $r_s$  and  $\lambda$ , there is a distinct Wigner crystal phase — also with a triangular lattice — which we call a halo Wigner crystal. A similar crystalline phase was recently studied in Bernal bilayer graphene [40]. To see this, we plot the momentum space occupation number  $n(\mathbf{k}) = \langle c_{\mathbf{k}}^\dagger c_{\mathbf{k}} \rangle$  for a normal Wigner crystal and a halo Wigner crystal in Fig. 3(a) and (b). We see that  $n(\mathbf{k} = 0)$  takes the maximal value for the normal Wigner crystal, while  $n(\mathbf{k} = 0) = 0$  for the halo Wigner crystal.

The vanishing of  $n(\mathbf{k} = 0)$  is in fact enforced by symmetry. We find these Wigner crystals have a  $C_3$  symmetry compatible with the triangular unit cell. Thus, viewing the Wigner crystal as a band insulator, the orbitals occupied at the high symmetry points must be eigenstates of the spatial symmetries, characterized by their angular momenta. Concretely, the  $C_3$  angular momentum is

$$\hat{C}_3 \psi_{\Gamma}^{\text{WC}} = \psi_{\Gamma}^{\text{WC}}, \quad \hat{C}_3 \psi_{\Gamma}^{\text{haloWC}} = e^{i2\pi/3} \psi_{\Gamma}^{\text{haloWC}}, \quad (14)$$

where  $\Psi_{\Gamma}$  is the single-particle orbital at the  $\Gamma$  point. Since the angular momentum at  $\Gamma$  does not depend on the choice of  $C_3$  centers, the halo Wigner crystal and the normal Wigner crystal are distinct crystalline insulators with different symmetry properties [41].

We can understand the change in angular momentum from a simple semiclassical analysis for the single particle problem [40]. Each individual semiclassical electron can be treated as a particle with dispersion and Berry curvature specified by Eq. (5). On top of that, it is subjected to a harmonic potential generated by the Coulomb interactions due to all other electrons present. The electron must follow the single-particle Schrodinger's equation in momentum space [42]:

$$\left( \epsilon_{\mathbf{k}} + \frac{\alpha}{2} |i\nabla_{\mathbf{k}} - \mathbf{A}_{\mathbf{k}}|^2 + \alpha \frac{\text{Tr } g_{\mu\nu}(\mathbf{k})}{2} \right) \psi_{\ell}(\mathbf{k}) = E_{\ell} \psi_{\ell}(\mathbf{k}). \quad (15)$$

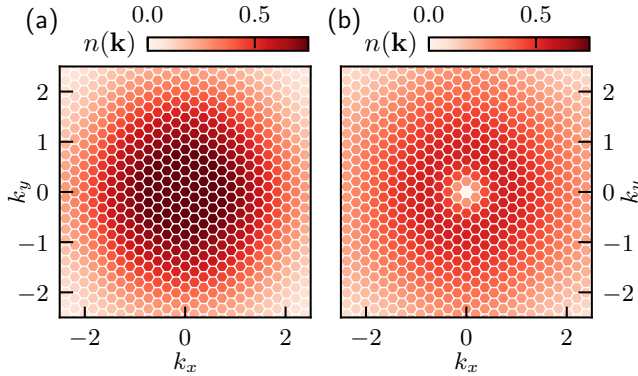


FIG. 3. Occupations of plane wave states in the lower band for different Wigner crystals. (a) Normal Wigner crystal at  $(r_s, \lambda) = (20, 0)$ . (b) halo Wigner crystal at  $(r_s, \lambda) = (20, 2.5)$ . The  $\mathbf{k} = 0$  region is depleted due to the Fock interactions at large  $\lambda$ .

Here, we approximated the confining potential by  $V(\mathbf{r}) = \alpha|\mathbf{r}|^2/2$ ,  $\mathbf{A}_\mathbf{k}$  is the Berry connection of the band, and  $g_{\mu\nu}(\mathbf{k})$  is the quantum metric of the band. When  $\lambda = 0$ , it reduces to the standard harmonic oscillator, whose ground state has angular momentum  $\ell = 0$ . When  $\lambda \rightarrow \infty$ , the Berry curvature is  $\Omega(\mathbf{k}) = 2\pi\delta(\mathbf{k})$ , corresponding to threading  $2\pi$  flux at the origin. Furthermore,  $\text{Tr } g_{\mu\nu}(\mathbf{k})$  becomes a delta function at the origin. These two effects collaborate to suppress the occupation of the  $\mathbf{k} = 0$  region and change the angular momentum of the ground state to  $\ell = 1$ , reproducing the numerical observation [43].

### C. Anomalous Hall Crystal

Due to the coexistence of single-particle Berry curvature and a trend towards crystallization at large interactions, we expect the anomalous Hall crystal (AHC) — a crystalline phase that becomes a Chern insulator when pinned — to appear. Previous works have emphasized the importance of nontrivial quantum geometry and Berry curvature in stabilizing the AHC phase [18–20, 23, 24, 29, 30]. In particular, Ref. [24] argued that enclosing more than  $\pi$  Berry curvature in the unit cell will tend to drive a transition from a WC to an AHC. For the  $\lambda$ -jellium, this Berry curvature can be approximated by the enclosed Berry curvature within the non-interacting Fermi surface, which is given by Eq. (9). The enclosed Berry curvature reaches  $I(k_F) = \pi$  at  $\lambda = 1/2$ , which is indeed roughly the location of the phase transition between WC and AHC at moderate  $r_s$ . At large  $r_s$ , the system is no longer weakly-coupled, and AHC is overtaken by the halo WC.

At even larger  $\lambda \gtrsim 2.5$ , the AHC undergoes a transition to the annular Fermi liquid. We note, however, that the large  $\lambda$  regime suffers from significant finite-size effects due to the tiny skyrmion core in momentum space.

Within the AHC phase, there is a subtle competition between different unit cell geometries, which we examine in Section V.

### IV. SECOND-ORDER TOPOLOGICAL PHASE TRANSITION BETWEEN AHC AND WC

We now examine the crystal-to-crystal phase transitions in  $\lambda$ -jellium, shown in Fig. 1(c). We diagnose the order of the phase transition from the direct gap of the Hartree-Fock band structure near the phase boundary. The transition from a normal WC to a halo WC is first order, consistent with its origin from level-crossing in the single-particle spectrum. The AHC to WC transition near  $\lambda = 1/2$  is also first order, similar to the first-order WC-AHC transition observed for RMG [23].

The transition between halo WC and AHC, on the other hand, appears to be continuous. Fig. 4(b) shows that as  $r_s$  approaches the transition from above, the mean-field charge gap closes in an unambiguously continuous manner. Approached from below, the charge gap closes but eventually jumps near the transition. We attribute this jump to finite-size effects, which become increasingly severe as one approaches the transition, requiring extremely fine grids and a large number of bands.

The origin of this continuous transition can be understood from the Hartree-Fock band structure in Fig. 4(a,b). There the bands are colored according to their spinor polarization  $z_a(\mathbf{k}) = \langle \psi_{a\mathbf{k}} | \sigma_z | \psi_{a\mathbf{k}} \rangle$ , where  $|\psi_{a\mathbf{k}}\rangle$  corresponds to the Bloch state at momentum  $\mathbf{k}$  of band  $a = 1, 2$ , counting from below. This thus reveals the band inversion nature of the transition: before the transition,  $z_1(\Gamma)$  is large whereas  $z_2(\Gamma)$  is small, but after the transition  $z_2(\Gamma)$  is large whereas  $z_1(\Gamma)$  is small. The vicinity of  $\Gamma$  is therefore well-described by a massive Dirac model. Tuning the mass through zero not only gives the observed band inversion, but also produces the angular momentum change required for the halo WC phase. The transition from the AHC to the halo WC is therefore captured by a standard Dirac mass closing.

We note that a similar transition has been analyzed in the context electrons in a magnetic field. Ref. [44] analyzed the phase transition between the “Hall crystal” phase [44–47] with a nonzero Chern number and the “Wigner crystal” phase with zero Chern number. Within the Hartree approximation, the transition was found to be precisely through the Dirac cone, suggesting the universality of this mechanism.

### V. AHC LATTICE GEOMETRY

In the *classical* Wigner crystal  $r_s \rightarrow \infty$ , the competition between different geometries is set purely through electrostatics, and the triangular lattice is preferred over the square lattice by about 0.5% [37]. This preference survives in the presence of quantum corrections, with the

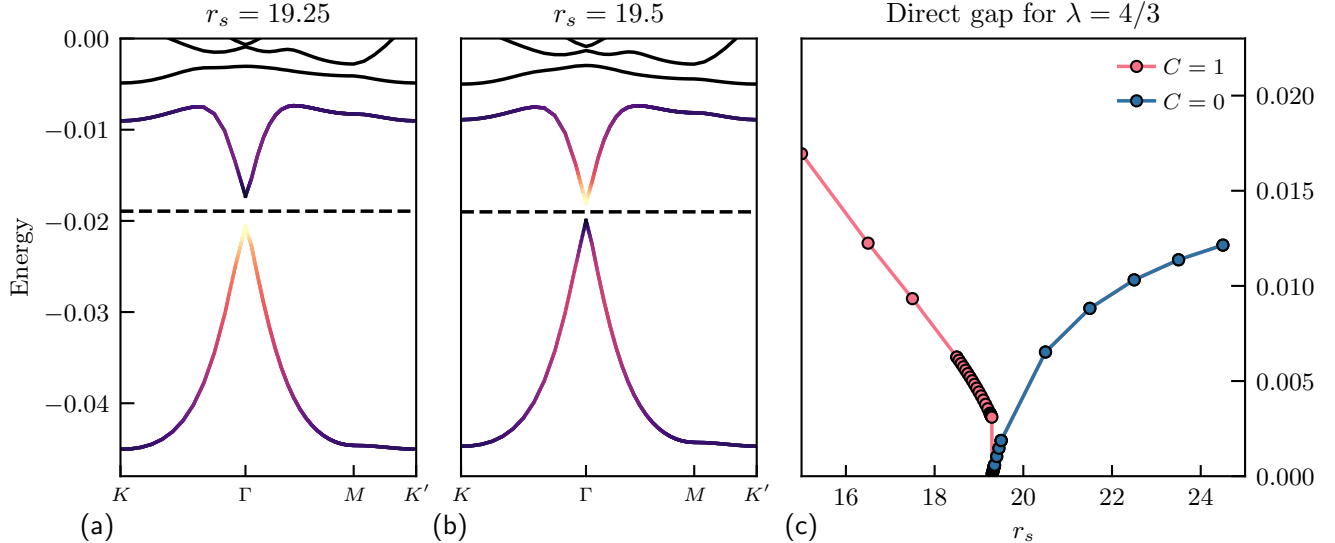


FIG. 4. Continuous phase transition driven by  $r_s$  at  $\lambda = 4/3$ . (a,b): self-consistent Hartree-Fock band structures before and after the transitions. Coloring corresponds to  $z_a(\mathbf{k})$ , the polarization on the first versus second spinor components. Clearly, the  $r_s$  tuned transition corresponds to a band inversion transition. (c): Direct charge gap near the phase boundary between AHC and the halo WC.

triangular Wigner crystal remaining favored all the way down to the Fermi liquid transition at  $r_s \approx 30$  [12]. However, there is a small region near  $r_s \approx 2$  in the spinful Wigner crystal, where a square lattice antiferromagnetic crystal is preferred at mean field level [13]. The preference for a triangular lattice therefore depends on the specific details of the Wigner crystal phase.

Does the AHC prefer a triangular lattice? To understand this, we turn to numerics and examine the energetic competition within the AHC phase between the triangular lattice and the square lattice. Our result, shown in Fig. 1(c), is that while the triangular lattice is preferred over the square in most of the AHC phase diagram, the reverse is true near the phase boundary between normal WC and AHC. The energetic competition remains close, with the square lattice favored by  $< 0.5\%$  at most at  $\lambda = 2/3$ . We note that finite-size energy corrections are significant, and methods detailed in Apps. B,C are required to compare the energies reliably. In contrast, the triangular lattice is more stable at larger  $\lambda$  and  $r_s$ . We caution that another unit cell shape may have yet-lower energy in this region; future work will examine the full landscape of possible unit cells [48].

The preference for the triangular lattice at large  $\lambda$  and moderate  $r_s$  can be understood from the single-particle wavefunctions. When  $\lambda \rightarrow \infty$ , the Berry curvature distribution becomes concentrated at  $\Gamma$ , which is similar to concentrated Berry curvature models of [49]. Electrons can thus be split into two groups: those in the small skyrmion core with Bloch momentum less than  $O(1/\lambda)$  — which carry all the topology — and topologically trivial ones away from the core. The trivial electrons dominate

the phase space and therefore control the leading order energetics. Thus, one expects that they will crystallize in a fashion similar to electrons in the jellium model, forming a triangular lattice. This argument is fully consistent with our empirical observation: the competition between the triangular and square lattices within the AHC phase is most relevant when  $\lambda$  is smallest.

## VI. DISCUSSION

In this paper, we proposed the  $\lambda$ -jellium model where a new parameter  $\lambda$  adds Berry curvature to the two-dimensional electron gas without modifying its quadratic dispersion. We investigated its phase diagram as a function of both  $\lambda$  and the standard potential/kinetic ratio  $r_s$  with self-consistent Hartree-Fock methods, finding a rich phase diagram, Fig 1(c). We find a large anomalous Hall crystal (AHC) phase, an electronic crystal that possesses a Chern number. Beyond that, increasing  $\lambda$  drives two transitions out of the usual Fermi liquid and Wigner crystal phases of the 2DEG. This is because  $\lambda$  produces a skyrmionic texture in the single-particle spinors, creating a “core” of mis-aligned spinors at large  $\lambda$ , incurring a significant exchange energy penalty. In the small  $r_s$  Fermi liquid, this makes occupying states close to zero momentum expensive, driving a circular-to-annular transition. At large  $r_s$ , the Wigner crystal transitions to a distinct “halo” Wigner crystal phase that depletes the  $\mathbf{k} = 0$  region as well. We also observed a continuous transition between crystals of different Chern numbers driven by  $r_s$ , similar to a phase transition analyzed in Ref. [44]. A

careful understanding of this transition and its experimental implications is left for a future work.

The presence of nontrivial Berry curvature in  $\lambda$ -jellium not only gives rise to topological states, but also changes the geometry of the crystalline ground states. While the usual Wigner crystal favors the triangular lattice, we found that in the  $\lambda$ -jellium model, AHC can favor the square lattice over the triangular lattice in some parts of the phase diagram.

A crucial next step is to move beyond mean-field techniques. As mentioned above, the two-component nature of our model together with the fact that only first and second derivatives appear make it well-suited for a variety of many-body numerical techniques, including variational monte carlo and neural network wavefunction methods.  $\lambda$ -jellium may therefore be a good model to establish crystallization with non-trivial Chern number

at the many-body level.

## ACKNOWLEDGMENTS

We thank Ophelia Evelyn Sommer, Taige Wang, Tianle Wang, Mike Zaletel, Patrick Ledwith and Es-Salam Khalaf for related collaborations and useful insights. We acknowledge Erez Berg, Yaar Vituri, Agnes Valenti, Miguel Morales, Shiwei Zhang, Félix Desrochers, Yong Baek Kim and Adrian Po for fruitful discussions. This research was supported in part by grant NSF PHY-2309135 to the Kavli Institute for Theoretical Physics (KITP). This research is funded in part by the Gordon and Betty Moore Foundation’s EPiQS Initiative, Grant GBMF8683 to T.S. A.V. and J.D. were funded by NSF DMR-2220703. DEP acknowledges startup funds from UC San Diego.

---

[1] E. Wigner. On the Interaction of Electrons in Metals. *Phys. Rev.*, 46(11):1002–1011, December 1934. Publisher: American Physical Society.

[2] Gabriele Giuliani and Giovanni Vignale. *Quantum Theory of the Electron Liquid*. Cambridge University Press, 2005.

[3] D. Ceperley. Ground state of the fermion one-component plasma: A monte carlo study in two and three dimensions. *Phys. Rev. B*, 18:3126–3138, Oct 1978.

[4] B Tanatar and David M Ceperley. Ground state of the two-dimensional electron gas. *Physical Review B*, 39(8):5005, 1989.

[5] Paola Gori-Giorgi, Saverio Moroni, and Giovanni B. Bachelet. Pair-distribution functions of the two-dimensional electron gas. *Phys. Rev. B*, 70:115102, Sep 2004.

[6] S. De Palo, M. Botti, S. Moroni, and Gaetano Senatore. Effects of thickness on the spin susceptibility of the two dimensional electron gas. *Phys. Rev. Lett.*, 94:226405, Jun 2005.

[7] D. Varsano, S. Moroni, and G. Senatore. Spin-polarization transition in the two-dimensional electron gas. *Europhysics Letters*, 53(3):348, feb 2001.

[8] Claudio Attaccalite, Saverio Moroni, Paola Gori-Giorgi, and Giovanni B. Bachelet. Correlation energy and spin polarization in the 2d electron gas. *Phys. Rev. Lett.*, 88:256601, Jun 2002.

[9] Francesco Rapisarda and Gaetano Senatore. Diffusion Monte Carlo study of electrons in two-dimensional layers. *Australian Journal of Physics*, 49:161, January 1996.

[10] N. D. Drummond and R. J. Needs. Phase diagram of the low-density two-dimensional homogeneous electron gas. *Phys. Rev. Lett.*, 102:126402, Mar 2009.

[11] N. D. Drummond and R. J. Needs. Quantum monte carlo study of the ground state of the two-dimensional fermi fluid. *Phys. Rev. B*, 79:085414, Feb 2009.

[12] Sam Azadi, N. D. Drummond, and S. M. Vinko. Quantum monte carlo study of the phase diagram of the two-dimensional uniform electron liquid, 2024.

[13] J. R. Trail, M. D. Towler, and R. J. Needs. Unrestricted hartree-fock theory of wigner crystals. *Phys. Rev. B*, 68:045107, Jul 2003.

[14] Zhengguang Lu, Tonghang Han, Yuxuan Yao, Aidan P Reddy, Jixiang Yang, Junseok Seo, Kenji Watanabe, Takashi Taniguchi, Liang Fu, and Long Ju. Fractional quantum anomalous hall effect in multilayer graphene. *Nature*, 626(8000):759–764, 2024.

[15] Jian Xie, Zihao Huo, Xin Lu, Zuo Feng, Zaizhe Zhang, Wenxuan Wang, Qiu Yang, Kenji Watanabe, Takashi Taniguchi, Kaihui Liu, Zhida Song, X. C. Xie, Jianpeng Liu, and Xiaobo Lu. Tunable fractional chern insulators in rhombohedral graphene superlattices, 2025.

[16] Dacen Waters, Ruiheng Su, Ellis Thompson, Anna Okounkova, Esmeralda Arreguin-Martinez, Minhao He, Katherine Hinds, Kenji Watanabe, Takashi Taniguchi, Xiaodong Xu, et al. Topological flat bands in a family of multilayer graphene moiré lattices. *Nature Communications*, 15(1):1–9, 2024.

[17] Zhengguang Lu, Tonghang Han, Yuxuan Yao, Zach Hadjiri, Jixiang Yang, Junseok Seo, Lihan Shi, Shenyong Ye, Kenji Watanabe, Takashi Taniguchi, and Long Ju. Extended quantum anomalous hall states in graphene/hbn moiré superlattices. *Nature*, 637(8048):1090–1095, January 2025.

[18] Junkai Dong, Taige Wang, Tianle Wang, Tomohiro Soejima, Michael P. Zaletel, Ashvin Vishwanath, and Daniel E. Parker. Anomalous hall crystals in rhombohedral multilayer graphene. i. interaction-driven chern bands and fractional quantum hall states at zero magnetic field. *Phys. Rev. Lett.*, 133:206503, Nov 2024.

[19] Boran Zhou, Hui Yang, and Ya-Hui Zhang. Fractional quantum anomalous hall effect in rhombohedral multilayer graphene in the moiréless limit. *Phys. Rev. Lett.*, 133:206504, Nov 2024.

[20] Zhihuan Dong, Adarsh S. Patri, and T. Senthil. Theory of quantum anomalous hall phases in pentalayer rhombohedral graphene moiré structures. *Phys. Rev. Lett.*, 133:206502, Nov 2024.

[21] Zhongqing Guo, Xin Lu, Bo Xie, and Jianpeng Liu. Fractional chern insulator states in multilayer graphene moiré

superlattices. *Physical Review B*, 110(7):075109, 2024.

[22] Yves H Kwan, Jiabin Yu, Jonah Herzog-Arbeitman, Dmitri K Efetov, Nicolas Regnault, and B Andrei Bernevig. Moiré fractional chern insulators iii: Hartree-fock phase diagram, magic angle regime for chern insulator states, the role of the moiré potential and goldstone gaps in rhombohedral graphene superlattices. *arXiv preprint arXiv:2312.11617*, 2023.

[23] Tomohiro Soejima, Junkai Dong, Taige Wang, Tianle Wang, Michael P. Zaletel, Ashvin Vishwanath, and Daniel E. Parker. Anomalous hall crystals in rhombohedral multilayer graphene. ii. general mechanism and a minimal model. *Phys. Rev. B*, 110:205124, Nov 2024.

[24] Zhihuan Dong, Adarsh S. Patri, and T. Senthil. Stability of anomalous hall crystals in multilayer rhombohedral graphene. *Phys. Rev. B*, 110:205130, Nov 2024.

[25] Jiabin Yu, Jonah Herzog-Arbeitman, Yves H Kwan, Nicolas Regnault, and B Andrei Bernevig. Moiré fractional chern insulators iv: Fluctuation-driven collapse of fcis in multi-band exact diagonalization calculations on rhombohedral graphene. *arXiv preprint arXiv:2407.13770*, 2024.

[26] Boran Zhou and Ya-Hui Zhang. New classes of quantum anomalous hall crystals in multilayer graphene, 2024.

[27] Valentin Crépel and Jennifer Cano. Efficient prediction of superlattice and anomalous miniband topology from quantum geometry. *Physical Review X*, 15(1):011004, 2025.

[28] B. Andrei Bernevig and Yves H. Kwan. "berry trashcan" model of interacting electrons in rhombohedral graphene, 2025.

[29] Yongxin Zeng, Daniele Guerci, Valentin Crépel, Andrew J. Millis, and Jennifer Cano. Sublattice structure and topology in spontaneously crystallized electronic states. *Phys. Rev. Lett.*, 132:236601, Jun 2024.

[30] Tixuan Tan and Trithep Devakul. Parent berry curvature and the ideal anomalous hall crystal. *Phys. Rev. X*, 14:041040, Nov 2024.

[31] Tixuan Tan, Julian May-Mann, and Trithep Devakul. Wavefunction approach to the fractional anomalous hall crystal, 2024.

[32] Félix Desrochers, Mark R. Hirsbrunner, Joe Huxford, Adarsh S. Patri, T. Senthil, and Yong Baek Kim. Elastic response and instabilities of anomalous hall crystals, 2025.

[33] Note that 1 Ry differs from the other standard measure of energy, a Hartree, by a factor of two.

[34] Jie Wang, Jennifer Cano, Andrew J. Millis, Zhao Liu, and Bo Yang. Exact landau level description of geometry and interaction in a flatband. *Phys. Rev. Lett.*, 127:246403, Dec 2021.

[35] Patrick J. Ledwith, Ashvin Vishwanath, and Daniel E. Parker. Vortexability: A unifying criterion for ideal fractional chern insulators. *Phys. Rev. B*, 108:205144, Nov 2023.

[36] R. J. Hunt, M. Szyniszewski, G. I. Prayogo, R. Maezono, and N. D. Drummond. Quantum monte carlo calculations of energy gaps from first principles. *Phys. Rev. B*, 98:075122, Aug 2018.

[37] Lynn Bonsall and A. A. Maradudin. Some static and dynamical properties of a two-dimensional wigner crystal. *Phys. Rev. B*, 15:1959–1973, Feb 1977.

[38] G. Meissner, H. Namaizawa, and M. Voss. Stability and image-potential-induced screening of electron vibrational excitations in a three-layer structure. *Phys. Rev. B*, 13:1370–1376, Feb 1976.

[39] Tsuneya Ando, Alan B. Fowler, and Frank Stern. Electronic properties of two-dimensional systems. *Rev. Mod. Phys.*, 54:437–672, Apr 1982.

[40] Sandeep Joy and Brian Skinner. Wigner crystallization in bernal bilayer graphene, 2023.

[41] Hoi Chun Po. Symmetry indicators of band topology. *Journal of Physics: Condensed Matter*, 32(26):263001, 2020.

[42] Hannah M. Price, Tomoki Ozawa, Nigel R. Cooper, and Iacopo Carusotto. Artificial magnetic fields in momentum space in spin-orbit-coupled systems. *Phys. Rev. A*, 91:033606, Mar 2015.

[43] We sincerely thank Ophelia Evelyn Sommer for pointing out the quantum metric contribution to us, which was missing in Ref. [40].

[44] Zlatko Tešanović, Françoise Axel, and B. I. Halperin. "Hall crystal" versus Wigner crystal. *Phys. Rev. B*, 39(12):8525–8551, April 1989. Publisher: American Physical Society.

[45] Steven Kivelson, C. Kallin, Daniel P. Arovas, and J. R. Schrieffer. Cooperative ring exchange theory of the fractional quantized Hall effect. *Phys. Rev. Lett.*, 56(8):873–876, February 1986. Publisher: American Physical Society.

[46] B. I. Halperin, Z. Tešanović, and F. Axel. Compatibility of Crystalline Order and the Quantized Hall Effect. *Phys. Rev. Lett.*, 57(7):922–922, August 1986. Publisher: American Physical Society.

[47] Steven Kivelson, C. Kallin, Daniel P. Arovas, and J. Robert Schrieffer. Cooperative ring exchange and the fractional quantum Hall effect. *Phys. Rev. B*, 36(3):1620–1646, July 1987. Publisher: American Physical Society.

[48] Junkai Dong, Ophelia Sommer, Tomohiro Soejima, Daniel Parker, and Ashvin Vishwanath. In preparation, 2025.

[49] Patrick J. Ledwith, Junkai Dong, Ashvin Vishwanath, and Eslam Khalaf. Nonlocal moments in the chern bands of twisted bilayer graphene, 2025.

[50] Masaaki Kawata and Masuhiro Mikami. Rapid calculation of two-dimensional ewald summation. *Chemical physics letters*, 340(1-2):157–164, 2001.

[51] DE Parry. The electrostatic potential in the surface region of an ionic crystal. *Surface Science*, 49(2):433–440, 1975.

[52] We could have gotten this result by noticing the charge distribution corresponding to this potential is nothing but a Gaussian.

## Appendix A: Modeling Details

This appendix describes modeling details of the two-dimensional topological electron gas.

### 1. Geometry

We consider electrons in the infinite plane subject to the Hamiltonian in Eq. (5) with a compensating background charge. To make the computation tractable, we impose a periodic boundary condition, and consider a Hilbert space defined by a finite torus  $M$  with area  $A = N\rho$ , where  $N$  is the number of particles. When imposing discrete translation symmetry, we choose  $M$  to be compatible with the choice of the Bravais lattice.

#### a. triangular lattice

Consider a direct lattice  $\mathbb{L}$  with lattice vectors

$$\mathbf{a}_1 = L \left( \frac{1}{2}, -\frac{\sqrt{3}}{2} \right), \quad \mathbf{a}_2 = L \left( \frac{1}{2}, \frac{\sqrt{3}}{2} \right). \quad (\text{A1})$$

Here  $L = \sqrt{\frac{2\pi}{\sqrt{3}}}a$  ensures the density  $\rho = \frac{1}{\pi a^2}$  matches the unit cell size  $A_{\text{uc}} = L^2 \frac{\sqrt{3}}{2}$ . The reciprocal lattice is  $\mathbb{L}^*$  with reciprocal basis vectors

$$\mathbf{g}_1 = \frac{2\pi}{L} \left( 1, -\frac{1}{\sqrt{3}} \right), \quad \mathbf{g}_2 = \frac{2\pi}{L} \left( 1, \frac{1}{\sqrt{3}} \right). \quad (\text{A2})$$

The full torus is a parallelogram with  $N = N_1 \times N_2$  unit cells and total area  $A = N A_{\text{uc}}$  with  $A_{\text{uc}} = \pi a^2$ .

#### b. Square lattice

The direct lattice is given by

$$\mathbf{a}_1 = L (1, 0), \quad \mathbf{a}_2 = L (0, 1). \quad (\text{A3})$$

Here we take  $L = \sqrt{\pi}a$ . The reciprocal lattice is  $\mathbb{L}^*$  with reciprocal basis vectors

$$\mathbf{g}_1 = \frac{2\pi}{L} (1, 0), \quad \mathbf{g}_2 = \frac{2\pi}{L} (0, 1). \quad (\text{A4})$$

The full torus is a parallelogram with  $N = N_1 \times N_2$  unit cells and total area  $A = N A_{\text{uc}}$  with  $A_{\text{uc}} = \pi a^2$ .

#### c. Brillouin Zone & Momentum Grid

We consider a parallelogram Brillouin zone

$$\text{BZ} = \{k_1 \mathbf{g}_1 + k_2 \mathbf{g}_2 : -\pi \leq k_{1,2} < \pi\}. \quad (\text{A5})$$

We denote elements of the Brillouin zone by  $\mathbf{k} \in \text{BZ}$ , and unrestricted momenta by  $\mathbf{q}$ . Such momenta can always be split as

$$\mathbf{q} = \{\mathbf{q}\} + [\mathbf{q}] = \mathbf{k} + \mathbf{g}, \quad (\text{A6})$$

where  $\mathbf{k}$  is in the first Brillouin zone and  $\mathbf{g} = n_1 \mathbf{g}_1 + n_2 \mathbf{g}_2$  is a reciprocal lattice vector.

We take a Monkhorst-Pack discretization of the Brillouin zone

$$\mathbf{k}_{n_1, n_2} = \frac{n_1 + \Phi_1/2\pi}{N_1} \mathbf{g}_1 + \frac{n_2 + \Phi_2/2\pi}{N_2} \mathbf{g}_2, \quad (\text{A7})$$

where  $0 \leq \Phi_{1,2} \leq 2\pi$  are the two fluxes through the torus and

$$n_i = \begin{cases} -\frac{N_i}{2}, -\frac{N_i}{2} + 1, \dots, \frac{N_i}{2} - 1 & \text{for } N_i \text{ even} \\ -\frac{N_i}{2} + \frac{1}{2}, -\frac{N_i}{2} + \frac{3}{2}, \dots, \frac{N_i}{2} - \frac{1}{2} & \text{for } N_i \text{ odd.} \end{cases} \quad (\text{A8})$$

This choice ensures that the lattice goes through  $\Gamma$  for  $\Phi_{1,2} = 0$ .

#### d. Momentum Shell Structure

To describe continuous functions within the unit cell (such as wavefunctions), we consider a “shell structure” of reciprocal momenta

$$S = \{\mathbf{g} = m_1 \mathbf{g}_1 + m_2 \mathbf{g}_2 : |\mathbf{g}| < N_s \max(|\mathbf{g}_1|, |\mathbf{g}_2|)\}. \quad (\text{A9})$$

In practice we usually take  $N_s = 5 - 7$ , giving  $|S| \approx 100 - 200$ .

## 2. First-Quantized Wavefunctions

We now set out basis conventions for first-quantized wavefunctions.

#### a. Microscopic Basis

Consider a microscopic basis  $|\mathbf{r}, I\rangle$  where  $I = 1, 2$  is a spinor index with corresponding basis vectors  $\check{e}_I$ . Wavefunctions are then written as

$$\psi^I(\mathbf{r}) = \langle \mathbf{r}, I | \psi \rangle. \quad (\text{A10})$$

Spinor indices are usually left implicit for concision.

#### b. Bloch Theorem Conventions

Suppose  $\hat{h}$  has discrete translation symmetry:  $[\hat{h}, \hat{T}_{\mathbf{R}}] = 0$  where  $\hat{T}_{\mathbf{R}} f(\mathbf{r}) = f(\mathbf{r} + \mathbf{R})$  is translation by a direct lattice vector. We then consider Bloch wavefunctions

$$\begin{aligned} \hat{h} |\phi_{\mathbf{k}n}\rangle &= \varepsilon_{\mathbf{k}n} |\phi_{\mathbf{k}n}\rangle \\ \hat{T}_{\mathbf{R}} |\phi_{\mathbf{k}n}\rangle &= e^{i\mathbf{k}\cdot\mathbf{r}} |\phi_{\mathbf{k}n}\rangle \\ \phi_{\mathbf{k}n}^I(\mathbf{r}) &= \langle \mathbf{r}, I | \psi_{\mathbf{k}n} \rangle. \end{aligned}$$

Here  $n$  labels bands. The periodic part of the Bloch waves are defined as

$$u_{\mathbf{k}n}^I(\mathbf{r}) = N^{\frac{1}{2}} e^{-i\mathbf{k}\cdot\mathbf{r}} \phi_{\mathbf{k}n}^I(\mathbf{r}), \quad (\text{A11})$$

normalized on the unit cell. These are eigenstates of  $\hat{h}[\mathbf{k}] = e^{-i\mathbf{k}\cdot\hat{\mathbf{r}}} \hat{h} e^{i\mathbf{k}\cdot\hat{\mathbf{r}}}$ . The Bloch states comprise a unitary transform:

$$\langle \phi_{\mathbf{k}n} | \phi_{\mathbf{k}'n'} \rangle = \sum_I \int_M d^2\mathbf{r} \overline{\phi_{\mathbf{k}n}^I(\mathbf{r})} \phi_{\mathbf{k}'n'}^I(\mathbf{r}) = \delta_{\mathbf{k}\mathbf{k}'} \delta_{nn'}, \quad (\text{A12})$$

$$\langle \mathbf{r}, I | \mathbf{r}', I' \rangle = \sum_n \sum_{\mathbf{k} \in \text{BZ}} \overline{\phi_{\mathbf{k}n}^I(\mathbf{r})} \phi_{\mathbf{k}n}^{I'}(\mathbf{r}') = \delta^{II'} \delta(\mathbf{r} - \mathbf{r}'). \quad (\text{A13})$$

Note that the  $\mathbf{k}$  sum is discrete due to the finite area  $A$ .

We adopt a periodic gauge so that

$$|\psi_{\mathbf{k}+\mathbf{g},n}\rangle = \hat{V}_{\mathbf{g}} |\psi_{\mathbf{k},n}\rangle, \quad \hat{V}_{\mathbf{g}} = e^{-i\mathbf{g}\cdot\hat{\mathbf{r}}}. \quad (\text{A14})$$

Though this operator is unitary in principle, in practice there is a parametrically small violation  $\hat{V}_{\mathbf{g}} \hat{V}_{\mathbf{g}}^\dagger = I + O(N_s)$ .

### c. Computational Basis

The computational basis is in momentum space, with unbounded momentum  $\mathbf{q}$  partitioned as  $\mathbf{k} + \mathbf{g}$  as above. Explicitly, we use

$$\langle \mathbf{r}, I | \mathbf{k}, \mathbf{g}, I' \rangle = \frac{1}{\sqrt{A}} e^{i(\mathbf{k}+\mathbf{g}) \cdot \mathbf{r}} \delta_{II'} \quad (\text{A15})$$

where  $\mathbf{g} = m_1 \mathbf{g}_1 + m_2 \mathbf{g}_2$  and  $\mathbf{k} \in \text{BZ}$ . The discretization of  $\mathbf{k}$  is given above, as is the cutoff on  $\mathbf{g}$ .

We use the following Fourier conventions:

$$\phi_{\mathbf{k}n}^I(\mathbf{r}) = \sum_{\mathbf{k}', \mathbf{g}, I'} \langle \mathbf{r}, I | \mathbf{k}', \mathbf{g}, I' \rangle \langle \mathbf{k}', \mathbf{g}, I' | \psi_{\mathbf{k},n} \rangle \quad (\text{A16})$$

$$= \frac{1}{\sqrt{A}} \sum_{\mathbf{g}} e^{i(\mathbf{k}+\mathbf{g}) \cdot \mathbf{r}} \phi_{\mathbf{k}n}^{\mathbf{g}I}, \quad (\text{A17})$$

$$\phi_{\mathbf{k},n}^{\mathbf{g},I} = \langle \mathbf{k}, \mathbf{g}, I | \psi_{\mathbf{k},n} \rangle = \sum_I \int_M d^2 \mathbf{r} \frac{e^{-i(\mathbf{k}+\mathbf{g}) \cdot \mathbf{r}}}{\sqrt{A}} \phi_{\mathbf{k},n}^I(\mathbf{r}). \quad (\text{A18})$$

The computational eigenvectors are thus normalized as

$$\sum_{\mathbf{g}, I} \overline{\phi_{\mathbf{k},n}^{\mathbf{g},I}} \phi_{\mathbf{k}',n'}^{\mathbf{g},I} = \delta_{nn'}. \quad (\text{A19})$$

### 3. Interactions

We consider Coulomb interactions between electrons

$$V(\mathbf{r}) = \frac{2}{r_s |\mathbf{r}|} = \frac{1}{A} \sum_{\mathbf{q}} V(\mathbf{q}) e^{i\mathbf{q} \cdot \mathbf{r}}, \quad (\text{A20})$$

$$V(\mathbf{q}) = \frac{4\pi}{r_s q}. \quad (\text{A21})$$

This Hamiltonian suffers from IR divergence due to the long-range Coulomb interaction, and thus needs to be accompanied by a neutralizing background charge. We review the procedure for correcting for neutralizing background charge in App. B. The resulting interaction on the torus takes the form

$$H_{\text{int}} = \frac{1}{2A} \sum_{\mathbf{q} \neq 0} V(\mathbf{q}) : \hat{\rho}_{\mathbf{q}} \hat{\rho}_{-\mathbf{q}} : + \Delta\epsilon, \quad (\text{A22})$$

where  $: \dots :$  is the normal ordering operator with respect to the vacuum. We remove  $\mathbf{q} = 0$  from the sum due to cancellation with the background charge, and  $\Delta\epsilon$  encodes the energy correction from self-images. Formally, it is written as

$$\Delta\epsilon = \frac{1}{N} \left( -\frac{\rho}{2} V_{\mathbf{q}=0} + \frac{1}{2} N \sum_{\mathbf{R} \neq 0} V(\mathbf{R}) \right), \quad (\text{A23})$$

where  $\mathbf{R}$  is the set of vectors that define the periodic boundary condition of the torus  $M$ . Although both of the terms are formally divergent, the divergences cancel each other. In practice, we need to perform an Ewald summation to compute this summation. Including the correction  $\Delta\epsilon$  handles the dominant contribution to finite-size energy correction of the system (see Fig. 5 below from the last Appendix).

#### 4. Second quantization and band projection

We now perform second quantization and band projection of the Hamiltonian. Let us denote by  $c_{\mathbf{k}}^\dagger$  the creation operator for the lower band. The kinetic part of the Hamiltonian is simply given by

$$H_{\text{kin}} = \sum_{\mathbf{k}} \frac{|\mathbf{k}|^2}{r_s^2} c_{\mathbf{k}}^\dagger c_{\mathbf{k}} \quad (\text{A24})$$

The non-constant part of the interaction is given by

$$\frac{1}{2A} \sum_{\mathbf{q} \neq 0} V(\mathbf{q}) : \hat{\rho}_{\mathbf{q}} \hat{\rho}_{-\mathbf{q}} : \quad (\text{A25})$$

We can write the band projected interaction as

$$\tilde{\rho}_{\mathbf{q}} = \sum_{\mathbf{k}} \Lambda_{\mathbf{q}}(\mathbf{k}) c_{\mathbf{k}}^\dagger c_{\mathbf{k}+\mathbf{q}} \quad (\text{A26})$$

where  $\Lambda_{\mathbf{q}}(\mathbf{k}) = \langle u_{\mathbf{k}} | u_{\mathbf{k}+\mathbf{q}} \rangle$ . The projected interaction is therefore written as

$$H_{\text{int}} = \frac{1}{2A} \sum_{\mathbf{q} \neq 0} \sum_{\mathbf{k}, \mathbf{k}'} V(\mathbf{q}) \Lambda_{\mathbf{q}}(\mathbf{k}) \Lambda_{-\mathbf{q}}(\mathbf{k}') : c_{\mathbf{k}}^\dagger c_{\mathbf{k}+\mathbf{q}} c_{\mathbf{k}'}^\dagger c_{\mathbf{k}'-\mathbf{q}} : . \quad (\text{A27})$$

#### Appendix B: Review of Ewald summation and Madelung energy

We now review the method of Ewald summation and computation of the Madelung energy. Some useful references are found in Ref. [50, 51].

We consider a system of electrons in the infinite plane. We denote their interaction by  $V(\mathbf{r})$ . The interaction energy is given by a formal sum

$$E_{\text{int}} = \sum_{i < j}^{\infty} V(\mathbf{r}_i - \mathbf{r}_j). \quad (\text{B1})$$

Our goal is to evaluate the energy density of this system by imposing periodic boundary condition. We consider a parallelogram  $P = \mathbf{R}_1 \wedge \mathbf{R}_2$  spanned by  $\mathbf{R}_1$  and  $\mathbf{R}_2$ . This defines the lattice  $\Lambda = \{m\mathbf{R}_1 + n\mathbf{R}_2 | m, n \in \mathbb{Z}\}$ . It is convenient to write  $\mathbf{R}_j = L_j \mathbf{r}_j$  with  $L_i \in \mathbb{Z}$ . We take  $|\hat{z} \cdot \mathbf{r}_1 \times \mathbf{r}_2| = 1/\rho$ , where  $\rho$  is the electron density. The parallelogram therefore contains  $N = L_1 L_2$  electrons.

We can now truncate the formal sum to define energy density. To do so, let us rewrite the formal sum as follows:

$$E_{\text{int}} = \sum_{i < j}^{\infty} V(\mathbf{r}_i - \mathbf{r}_j) \quad (\text{B2})$$

$$= \frac{1}{2} \sum_{i \neq j}^{\infty} V(\mathbf{r}_i - \mathbf{r}_j) \quad (\text{B3})$$

$$= \frac{1}{2} \sum_{i \neq j}^N \sum_{\mathbf{R}_a, \mathbf{R}_b \in \Lambda} V(\mathbf{r}_i - \mathbf{R}_a - \mathbf{r}_j - \mathbf{R}_b) + \frac{1}{2} \sum_i^N \sum_{\mathbf{R}_a \neq \mathbf{R}_b} V(\mathbf{R}_a - \mathbf{R}_b) \quad (\text{B4})$$

$$= \sum_{\mathbf{R}_a \in \Lambda} \frac{1}{2} \sum_{i \neq j}^N \sum_{\mathbf{R}_b \in \Lambda} V(\mathbf{r}_i - \mathbf{r}_j - \mathbf{R}_b) + \sum_{\mathbf{R}_a} \frac{1}{2} \sum_i^N \sum_{\mathbf{R}_b \neq 0} V(\mathbf{R}_b) \quad (\text{B5})$$

$$= \sum_{\mathbf{R}_a} \left( \sum_{i < j}^N \sum_{\mathbf{R}_b \in \Lambda} V(\mathbf{r}_i - \mathbf{r}_j - \mathbf{R}_b) + \frac{1}{2} \sum_i^N \sum_{\mathbf{R}_b \neq 0} V(\mathbf{R}_b) \right) \quad (\text{B6})$$

In going from the second line to the third line, we introduced the sum over positions within the unit cell i.e.  $\sum_i^\infty f(\mathbf{r}_i)$  is the sum over all particle positions, and  $\sum_i^N f(\mathbf{r}_i)$  is a sum over particle positions within the unit cell. We can split the sum to the part  $i \neq j$ , in which case there is no restriction on values of  $\mathbf{R}_a$  and  $\mathbf{R}_b$ , and  $i = j$ , in which case we require  $\mathbf{R}_a \neq \mathbf{R}_b$ . The energy per particle is then given by

$$\epsilon_{\text{int}} = \frac{1}{N} \left( \sum_{i < j}^N \sum_{\mathbf{R} \in \Lambda} V(\mathbf{r}_i - \mathbf{r}_j - \mathbf{R}) + \frac{1}{2} \sum_i^N \sum_{\mathbf{R} \neq 0} V(\mathbf{R}) \right), \quad (\text{B7})$$

where  $\mathbf{r}_i$ 's label the location of  $N$  electrons within the parallelogram.

If  $V(\mathbf{r})$  is the Coulomb interaction, this sum is infrared divergent. We can regularize this divergence by adding a neutralizing background:

$$\epsilon_{\text{bkg}} = \frac{1}{N} \left( - \sum_i^N \int \rho_b(\mathbf{r}) V(\mathbf{r}) d^2 r + \frac{1}{2} \int_P d^2 \mathbf{r} \int_{\mathbb{R}^2} d^2 \mathbf{r}' \rho_b(\mathbf{r}) \rho_b(\mathbf{r}') V(\mathbf{r} - \mathbf{r}') \right) \quad (\text{B8})$$

$$= \frac{1}{N} \left( -N\rho \int V(\mathbf{r}) d^2 \mathbf{r} + \frac{1}{2} \frac{N}{\rho} \rho^2 \int d^2 \mathbf{r} V(\mathbf{r}) \right) \quad (\text{B9})$$

$$= -\rho \int V(\mathbf{r}) d^2 \mathbf{r} + \frac{1}{2} \int d^2 \mathbf{r} V(\mathbf{r}) = -\frac{\rho}{2} \int d^2 \mathbf{r} V(\mathbf{r}) \quad (\text{B10})$$

where we have chosen the neutralizing background to be uniform and exactly cancel the charges of the electrons:  $\rho_b(\mathbf{r}) = \rho$ . In the sum, the first term is the electron-background interaction, and the second term is the background-background interaction.

We now wish to evaluate this expression in momentum space. To do so, we first assume  $V(r)$  is properly regularized such that  $V(\mathbf{k} = 0) = \int d^2 \mathbf{r} V(\mathbf{r})$  is finite. The precise regularization scheme does not matter. The interaction term can then be rearranged as

$$\epsilon_{\text{int}} = \frac{1}{N} \left( \sum_{i < j}^N \sum_{\mathbf{R} \in \Lambda} V(\mathbf{r}_i - \mathbf{r}_j - \mathbf{R}) + \frac{1}{2} \sum_i^N \sum_{\mathbf{R} \neq 0} V(\mathbf{R}) \right) \quad (\text{B11})$$

$$= \frac{1}{N} \left( \frac{1}{|P|} \sum_{i < j}^N \sum_{\mathbf{G} \in \Lambda^*} \tilde{V}(\mathbf{G}) e^{i\mathbf{G} \cdot (\mathbf{r}_i - \mathbf{r}_j)} + \frac{1}{2} \sum_i^N \sum_{\mathbf{R} \neq 0} V(\mathbf{R}) \right) \quad (\text{B12})$$

$$= \frac{1}{N} \left( \frac{(N-1)\rho}{2} \tilde{V}(0) + \frac{\rho}{N} \sum_{i < j}^N \sum_{\mathbf{G} \neq 0} \tilde{V}(\mathbf{G}) e^{i\mathbf{G} \cdot (\mathbf{r}_i - \mathbf{r}_j)} + \frac{1}{2} \sum_i^N \sum_{\mathbf{R} \neq 0} V(\mathbf{R}) \right) \quad (\text{B13})$$

where we used Poisson summation:  $\sum_{\mathbf{R} \in \Lambda} f(\mathbf{R}) = \frac{1}{|P|} \sum_{\mathbf{G} \in \Lambda^*} \tilde{f}(\mathbf{G})$ ,  $|P| = N/\rho$ . From now on, we will switch to the notation where  $\tilde{f}$  is the Fourier transform of  $f$ . The neutralizing background, on the other hand, gives

$$\epsilon_{\text{bkg}} = -\frac{\rho}{2} \int d^2 \mathbf{r} V(\mathbf{r}) = -\frac{1}{2} \rho \tilde{V}(0). \quad (\text{B14})$$

Combining these together, we get

$$\epsilon_{\text{int}} + \epsilon_{\text{bkg}} = \frac{1}{N} \left( -\frac{\rho}{2} \tilde{V}(0) + \frac{\rho}{N} \sum_{i < j}^N \sum_{\mathbf{G} \neq 0} \tilde{V}(\mathbf{G}) e^{i\mathbf{G} \cdot (\mathbf{r}_i - \mathbf{r}_j)} + \frac{1}{2} \sum_i^N \sum_{\mathbf{R} \neq 0} V(\mathbf{R}) \right) \quad (\text{B15})$$

The first term and the last term (Madelung term) do not scale with the number of particles  $N$ , so they can be dropped to give us

$$\epsilon_{\text{int}} + \epsilon_{\text{bkg}} = \frac{\rho}{N^2} \sum_{i < j}^N \sum_{\mathbf{G} < 0} \tilde{V}(\mathbf{G}) e^{i\mathbf{G} \cdot (\mathbf{r}_i - \mathbf{r}_j)} + O\left(\frac{1}{N}\right). \quad (\text{B16})$$

We now treat the  $O(1/N)$  term carefully to tame the finite-size effect. The correction term is

$$\Delta\epsilon = \frac{1}{N} \left( -\frac{\rho}{2} \tilde{V}(0) + \frac{1}{2} N \sum_{\mathbf{R} \neq 0} V(\mathbf{R}) \right). \quad (\text{B17})$$

We will now use the Ewald summation trick and split the interaction as  $V(r) = V^\ell(r) + V^s(r)$ . We demand  $V^\ell(0) < \infty$  (UV convergent, IR divergent) and  $\tilde{V}^s(k=0) < \infty$  (UV divergent, IR convergent). We can now rewrite the sum as

$$\Delta\epsilon = \frac{1}{N} \left( -\frac{\rho}{2} \tilde{V}^\ell(0) + \frac{1}{2} N \sum_{\mathbf{R} \neq 0} V^\ell(\mathbf{R}) - \frac{\rho}{2} \tilde{V}^s(0) + \frac{1}{2} N \sum_{\mathbf{R} \neq 0} V^s(\mathbf{R}) \right) \quad (\text{B18})$$

$$= \frac{1}{N} \left( -\frac{\rho}{2} \tilde{V}^\ell(0) + \frac{1}{2} N \sum_{\mathbf{R}} V^\ell(\mathbf{R}) - \frac{N}{2} V^\ell(0) - \frac{\rho}{2} \tilde{V}^s(0) + \frac{1}{2} N \sum_{\mathbf{R} \neq 0} V^s(\mathbf{R}) \right) \quad (\text{B19})$$

$$= \frac{1}{N} \left( -\frac{\rho}{2} \tilde{V}^\ell(0) + \frac{\rho}{2} \sum_{\mathbf{G}} \tilde{V}^\ell(\mathbf{G}) - \frac{N}{2} V^\ell(0) - \frac{\rho}{2} \tilde{V}^s(0) + \frac{1}{2} N \sum_{\mathbf{R} \neq 0} V^s(\mathbf{R}) \right) \quad (\text{B20})$$

$$= \frac{1}{N} \left( \frac{\rho}{2} \sum_{\mathbf{G} \neq 0} \tilde{V}^\ell(\mathbf{G}) - \frac{N}{2} V^\ell(0) - \frac{\rho}{2} \tilde{V}^s(0) + \frac{1}{2} N \sum_{\mathbf{R} \neq 0} V^s(\mathbf{R}) \right) \quad (\text{B21})$$

All terms in this expression are manifestly finite, and we can evaluate them directly.

### 1. Error function for the Ewald trick

We now make a choice for decomposition  $V(\mathbf{r}) = V(|\mathbf{r}|) = V^\ell(|\mathbf{r}|) + V^s(|\mathbf{r}|)$ . The standard method is to take the following:

$$V^s(r) = \frac{\text{erfc}(\alpha r)}{r}, \quad V^\ell(r) = \frac{\text{erf}(\alpha r)}{r}, \quad (\text{B22})$$

where  $\text{erf}(r) = \frac{2}{\sqrt{\pi}} \int_0^r e^{-t^2} dt$ ,  $\text{erfc}(r) = 1 - \text{erf}(r)$ . There is a simple physical picture for this choice.  $V^\ell(r)$  is the potential coming from a gaussian cloud of electron with charge density  $e^{-\alpha r^2}$ , as can be checked from the Gauss law.

### 2. 3D Ewald

Even though we are interested in 2D, it is convenient to start from evaluating the 3D integral first. The 3D Fourier transform of  $V^\ell(r)$  is

$$\tilde{V}^\ell(k) = 4\pi \frac{e^{-\frac{k^2}{4\alpha^2}}}{k^2} \quad (\text{B23})$$

We check this by performing Fourier transform:

$$\mathcal{F}[\tilde{V}^\ell](r) = 4\pi \int \frac{d^3k}{(2\pi)^3} \frac{e^{-\frac{k^2}{4\alpha^2}}}{k^2} e^{ik \cdot r} \quad (B24)$$

$$= \frac{1}{\pi} \int_0^\infty dk e^{-\frac{k^2}{4\alpha^2}} \int \sin \theta d\theta e^{ik|r| \cos \theta} \quad (B25)$$

$$= 4\pi \frac{1}{\pi} \int_0^\infty dk \frac{1}{ik|r|} [e^{ik|r|} - e^{-ik|r|}] e^{-\frac{k^2}{4\alpha^2}} \quad (B26)$$

$$= \frac{1}{\pi|r|} \int_{-\infty}^\infty dk \frac{1}{ik} e^{ik|r|} e^{-\frac{k^2}{4\alpha^2}} \quad (B27)$$

Let  $I(r) = \int_{-\infty}^\infty dk \frac{1}{ik} e^{ik|r|} e^{-\frac{k^2}{4\alpha^2}}$ . Then

$$\frac{dI(r)}{dr} = \int_{-\infty}^\infty dk e^{ik|r|} e^{-\frac{k^2}{4\alpha^2}} = 2\alpha\sqrt{\pi} e^{-\alpha^2|r|^2} \implies I(r) = 2\sqrt{\pi} \int_0^{\alpha r} e^{-t^2} dt = \pi \operatorname{erf}(\alpha r) \quad (B28)$$

So we have  $\mathcal{F}[\tilde{V}^\ell](r) = I(r)/\pi r = V^\ell(r)$ . [52]

### 3. 2D Ewald

We will now perform 2D Ewald transform. We start from the 3D Fourier transform of the long range potential.

$$\tilde{V}^\ell(k) = 4\pi \frac{e^{-\frac{k^2}{4\alpha^2}}}{k^2} \quad (B29)$$

We can now integrate this in the  $z$  direction to get 2D Fourier component:

$$\tilde{V}_{2D}^\ell(k) = e^{-\frac{|k|^2}{4\alpha^2}} \int_{-\infty}^\infty \frac{dk_z}{2\pi} e^{-\frac{k_z^2}{4\alpha^2}} \frac{4\pi}{k^2 + k_z^2} \quad (B30)$$

We use the following standard integral equality:

$$\int_0^\infty dk \frac{e^{-k^2}}{k^2 + t^2} = \frac{\pi \operatorname{erfc}(t)}{2t} e^{t^2} \quad (B31)$$

Using this, we get

$$\tilde{V}_{2D}^\ell(k) = \frac{2\pi \operatorname{erfc}(\frac{k}{2\alpha})}{k} \quad (B32)$$

Rather interestingly, the error function shows up in real space instead of momentum space in this case. We can also evaluate the integral of the short-range part of the interaction:

$$\int d^2r \frac{\operatorname{erfc}(\alpha r)}{r} = 2\pi \int_0^\infty dr \operatorname{erfc}(\alpha r) = \frac{2\sqrt{\pi}}{\alpha} \quad (B33)$$

The spatial limit of the interaction is easy to see. As  $\operatorname{erf}(r) = 2r/\sqrt{\pi} + O(r^3)$ , we have

$$V^\ell(0) = \frac{2\alpha}{\sqrt{\pi}} \quad (B34)$$

Combining these results together, the energy correction using Ewald summation is given by

$$\Delta\epsilon_C = \frac{1}{N} \left( \frac{\rho}{2} \sum_{\mathbf{G} \neq 0} \frac{2\pi \operatorname{erfc}(\frac{k}{2\alpha})}{k} - \frac{N}{2} \frac{2\alpha}{\sqrt{\pi}} - \frac{\rho}{2} \frac{2\sqrt{\pi}}{\alpha} + \frac{1}{2} N \sum_{\mathbf{R} \neq 0} \frac{\operatorname{erfc}(\alpha R)}{R} \right). \quad (\text{B35})$$

For 2D electron gas in particular, in which the interaction is given by  $\frac{2}{r_s}$ , we have

$$\Delta\epsilon_{2DEG} = \frac{2}{Nr_s} \left( \frac{\rho}{2} \sum_{\mathbf{G} \neq 0} \frac{2\pi \operatorname{erfc}(\frac{k}{2\alpha})}{k} - \frac{N}{2} \frac{2\alpha}{\sqrt{\pi}} - \frac{\rho}{2} \frac{2\sqrt{\pi}}{\alpha} + \frac{1}{2} N \sum_{\mathbf{R} \neq 0} \frac{\operatorname{erfc}(\alpha R)}{R} \right), \quad (\text{B36})$$

where the  $\mathbf{r}_j$  must be chosen to have area  $\pi$ . These summations can then be performed easily by choosing an appropriate  $\alpha$  and truncating the summation at finite  $|\mathbf{G}|$  and  $|\mathbf{R}|$ , which only leaves an exponentially small error.

## Appendix C: Hartree-Fock procedure

We use standard self-consistent Hartree-Fock calculations to obtain the SCHF ground state of the electronic system.

### 1. Continuous translation symmetry

In the presence of continuous symmetry, the mean-field states are fully characterized by  $n(k)$ , and its energies are given by Eq. (10) (12), which reproduce for convenience below:

$$E_{\text{kin}} = \sum_{\mathbf{k}} n(\mathbf{k}) \frac{|\mathbf{k}|^2}{r_s^2}, \quad (\text{C1})$$

$$E_{\text{int}} = -\frac{1}{2A} \sum_{\mathbf{k}, \mathbf{k}'} \tilde{V}(\mathbf{k}, \mathbf{k}') n(\mathbf{k}) n(\mathbf{k}'). \quad (\text{C2})$$

This simple formula allows us to evaluate the energy of Fermi liquid candidate states efficiently. As our Fermi liquid ansatz, we take the following  $n(k)$ :

$$n(k) = \begin{cases} 0 & k < k_{\min} \\ 1 & k_{\min} \leq k \leq k_{\max} \\ 0 & k > k_{\max} \end{cases}. \quad (\text{C3})$$

Here  $k_{\max}^2 - k_{\min}^2 = 4/a^2$  to ensure the same electron density. Setting  $k_{\min} = 0$  recovers the circular Fermi surface. By minimizing the sum of kinetic and interaction energy with respect to  $k_{\min}$ , we can evaluate the energy of the Fermi liquid. This reduces to evaluating numerical integrals, which allows us to achieve the thermodynamic limit at a small energy cost.

### 2. Discrete translation symmetry

We now consider performing the self-consistent Hartree Fock while only imposing discrete translation symmetry. As usual, we consider single-particle density matrices  $P(\mathbf{k})_{\beta\alpha} = \langle c_{\mathbf{k}\beta}^\dagger c_{\mathbf{k}\alpha} \rangle$ , where  $\alpha$  and  $\beta$  are collective indices for valley, spin, and band. These density matrices are in one-to-one correspondence with Slater determinant states. We define the Hartree and Fock Hamiltonians as

$$h_H[P](\mathbf{k}) = \frac{1}{A} \sum_{\mathbf{g}} V(\mathbf{g}) \Lambda_{\mathbf{g}}(\mathbf{k}) \left( \sum_{\mathbf{k}} \operatorname{Tr}[P(\mathbf{k}) \Lambda_{\mathbf{g}}(\mathbf{k})^\dagger] \right) \quad (\text{C4a})$$

$$h_F[P](\mathbf{k}) = -\frac{1}{A} \sum_{\mathbf{q}} V(\mathbf{q}) \Lambda_{\mathbf{q}}(\mathbf{k}) P([\mathbf{k} + \mathbf{q}]) \Lambda_{\mathbf{q}}(\mathbf{k})^\dagger \quad (\text{C4b})$$

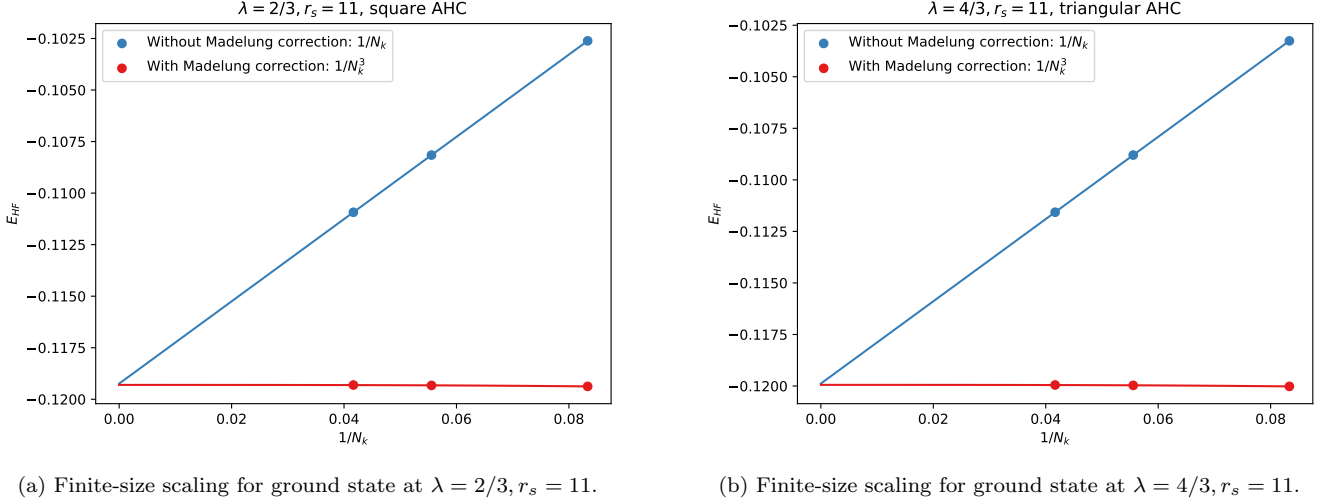


FIG. 5. Finite-size scaling plots for the square and triangular AHC states, with and without the Madelung correction. The Madelung correction significantly reduces the finite-size effect.

where  $[\Lambda_{\mathbf{q}}(\mathbf{k})]_{\alpha\beta} = \langle \psi_{\mathbf{k}\alpha} | e^{-i\mathbf{q}\cdot\mathbf{r}} | \psi_{\mathbf{k}+\mathbf{q}\beta} \rangle$  are form factors, and are treated as matrices whose labels are identical to the single-particle ones. The sum over  $\mathbf{g}$  runs over reciprocal vectors while  $\mathbf{q}$  runs over all momentum transfers. Via Wick's theorem, the energy of the Slater-determinant state is

$$E[P] = \frac{1}{2} \text{Tr}[P(2h_{\text{kin}} + h_H[P] + h_F[P])] \quad (\text{C5})$$

where the trace is over momentum and all other band labels.

We use the optimal-damping algorithm (ODA) to converge to states satisfying the self-consistency condition

$$[P, h_{\text{kin}} + h_H[P] + h_F[P]] = 0 \quad (\text{C6})$$

to tolerances approaching the square root of machine precision (i.e. machine precision in  $E[P]$ ). We use Monkhorst-Pack grids with  $12 \times 12$  up to  $36 \times 36$  unit cells, and ensure that the range of momentum transfers  $\mathbf{q}$  considered is sufficiently large to converge the energy of the state, out to several Brillouin zone sizes. The choices of system sizes  $N_k$  are always multiples of 6 to ensure that the high-symmetry points, such as the  $M$  and  $K$  points when the lattice is triangular, are properly sampled. We further truncate the single-particle Hilbert spaces to  $N_b = 7, 13, 19, 37$  bands, until energy convergence is reached. To avoid non-global minima, we initialize SCHF in a variety of states for each parameter point using a mix of physical ansätze as well as random initial states.

#### Appendix D: Finite-size scaling of the energy

In this section, we detail how we perform finite-size scaling.

As discussed in App. C 1, our energy evaluation is already in the thermodynamic limit, and therefore does not require finite-size scaling.

As for the Hartree-Fock ground states found for discrete translation symmetry, we take into account the finite-size corrections detailed in App. B:

$$E_{\text{corrected}}[P] = E[P] + \frac{2}{r_s} \Delta\epsilon_C, \quad (\text{D1})$$

where  $\Delta\epsilon_C$  is given by Eq. (B35). This improves the convergence of energies greatly, from a  $1/L$  asymptotic to a  $1/L^3$  asymptotic [36]. In Fig. 5a, 5b, we show the result of such finite-size scaling. The inclusion of the Madelung energy correction indeed reduces the finite-size effect considerably.